EVALUATION OF A RANGE OF MODELING APPROACHES FOR UAV UNSTEADY AERODYNAMICS

Brenden Oates, Georgia Institute of Technology, Atlanta, GA, USA
Pyae Su, Georgia Institute of Technology, Atlanta, GA, USA
John T. Hrynuk, DEVCOM Army Research Laboratory, Aberdeen, MD, USA
Marilyn J. Smith, Georgia Institute of Technology, Atlanta, GA, USA
Juergen Rauleder, Georgia Institute of Technology, Atlanta, GA, USA

Abstract

Rotary-wing vehicle development and application have expanded in the past two decades to include a multitude of configurations and operational environments. More efficient approaches to obtain vehicle flight characteristics during design, as well as for modeling and simulation, are needed to augment traditional approaches such as wind tunnel testing and high-fidelity unsteady Reynolds-Averaged Navier–Stokes (uRANS) computational fluid dynamics (CFD). This effort details the evaluation of the ability of two approaches, solutions to the Lattice–Boltzmann equations and a physics-based reduced-order model, to predict the airloads on an uncrewed aerial vehicle (UAV), correlated with CFD and wind tunnel tests. The sensitivity of differences observed in these predictions is quantified through a flight simulation code designed for vehicle design and simulation.

1. NOTATION

A	Reference area, $A = l_{ref}^2$, m^2
C_L	Lift coefficient, $C_L = L/q_\infty A$
C_D	Drag coefficient, $C_D = D/q_\infty A$
C_Y	Side force coefficient, $C_Y = Y/q_\infty A$
l_{ref}	Reference length, m
D	Drag Force, N
L	Lift Force, N
q_∞	Dynamic pressure, N/m^2
Y	Side Force, N
α	Angle of attack, deg.
β	Yaw angle, deg.
ω	Vorticity, 1/s

2. INTRODUCTION

Uncrewed Aerial Vehicles (UAVs) are playing increasingly important roles in both civilian applications and military operations (Ref. 1). Without the constraint of an onboard pilot (or passengers), these vehicles are capable of rapid, aggressive maneuvering (Ref. 2) solely or with other crewed and uninhabited vehicles (Ref. 3).

Aerodynamics play a critical role in structural assessment and power consumption of these systems. In the past, much effort has been focused on the development of increasingly detailed analyses, specifically solutions of the unsteady Reynolds-Averaged Navier–Stokes (uRANS) equations. With the expansion of computer hardware capabilities and improved software such as advanced transition algorithms (e.g., Refs. 4–6), turbulence closures (e.g., Refs. 7, 8) and Cartesian wake models (e.g., Ref. 9), uRANS CFD can deliver detailed physics results for a static orientation in hours on large-scale high-performance computing (HPC) clusters with sufficient cores.

While these uRANS advances are breaking new ground in the understanding of the complex physics of these vehicles, their usage in design, where quick turnaround times for tens or hundreds of configurations are required, or in real-time modeling and simulation (M&S) is limited at this stage due to their computational expense. Research and development (R&D) efforts continue to address these gaps through a number of different avenues. For example, dual-solver hybrid methods resolve the more expensive Navier–Stokes solutions only in the near body to generate the wake vorticity strength and magnitude. URANS is replaced in the wake with the more efficient solution of potential or vorticity-velocity RANS equations, as reviewed by Smith and Moushegian (Ref. 10). These methods avoid the rapid wake dissipation that occurs with uRANS, without significant mesh and timestep refinement (e.g., Ref. 11), in particular in hover.

The prior examples of reducing costs are useful in detailed design phases, but still have a trade-off between large computer systems and wall-clock time to achieve their solutions. Fast aerodynamic models capable of predicting the vehicle behavior in highly dynamic environments, such as urban canyons with wind conditions or shipboard terminal operations, are needed for control law design, as well as for M&S to improve safety through enhanced pilot training or to help with the investigations of ship-aircraft operating limits. These models should be capable of including the unsteady physics associated with these new (and potentially widely varying) designs, rather than relying on surrogate models trained on a specific design.

Improved accuracy in current M&S models is critical for more maneuverable systems. Traditional approaches relegate the fuselage aerodynamics to a point mass or simple equivalent flat plate drag. They further neglect interference effects between rotors and fuselages, as well as between body components. These traditional assumptions have been shown to be significantly less accurate in predicting maneuver responses when compared to CFD and reduced-order models that include these effects (Ref. 12–17). These inaccuracies can lead to operations that do not fully exploit the vehicle capabilities or, conversely, lead to safety concerns near obstacles, particularly in terminal operations.

The US Navy DIVE program, among other efforts, has expended significant efforts in developing very high fidelity approaches with uRANS CFD coupled to a dynamic interface (DI). Smaller meshes are required by uRANS CFD to maintain low latency between the DI and CFD (Ref. 18). This suggests that alternate, more efficient computational approaches using uRANS CFD, such as those described earlier (Ref. 19, 20) or, alternatively, computational approaches that resolve a different set of equations, such as the Lattice–Boltzmann equations, may be more effective.

The Lattice-Boltzmann method (LBM), due to its highly parallelizable nature, can be rapidly accelerated using modern general-purpose graphical processing units (GPGPUs). Studies have investigated the capabilities of GPU-accelerated LBM for helicopter aerodynamics and demonstrated the LBM's suitability as a mid-fidelity method for rotorcraft flows (Ref. 21–24). Oates et al. (Ref. 25) have shown that LBM offers a significant increase in computational efficiency compared to RANS DDES CFD when a trade-off in accuracy is acceptable.

Given the widely varying requirements for different applications, the most efficient and appropriate level of aerodynamic fidelity should be selected for a given application. The accuracy of each method and the characteristics that each method present are important when determining which method to utilize. There is a trade-off, however, between the accuracy of a method and the computational expense and time that it takes to generate results that are feasible and converged. It is also important to consider the requisite effort to initialize or preprocess the vehicle simulation when evaluating these different approaches.

This paper examines and compares the accuracy and computational cost between three levels of aerodynamic model fidelity that are of interest across the spectrum of real-time simulation, design, and detailed analysis. For the analysis, a reduced-order, physics-based solver, the Georgia Tech Aerodynamics of Bluff Bodies (GTABB) (Ref. 15, 17, 26, 27), a Lattice–Boltzmann Method (LBM), and uRANS CFD were compared with one another and correlated with experimental results from wind tunnel measurements. These measurements included integrated vehicle forces and moments, and flow field measurements using time-resolved particle image velocimetry (PIV). A simplified, fundamental quad-rotor UAV without propellers was selected as the test case. In addition to the integrated loads and moments of the vehicle, the flow field topology and coherent structures are examined across analysis methods and compared to the experiment.

3. TECHNICAL APPROACH

To evaluate and validate the different levels of model fidelity, the three computational methods (COMPASS, LBM, FUN3D) were compared to experimental aerodynamic load data, as well as flow field visualizations obtained at the DEVCOM Army Research Laboratory (ARL) wind tunnel. A notional UAV, pictured in Fig. 1, was evaluated both computationally and experimentally. In this effort, the 75% scale model was evaluated at a flight speed of 20 m/s to minimize blockage while maximizing the load cell capability. No rotors were included in this analysis as the methodology for predicting the rotor behavior would, in a simulation method, be the same no matter the source from which the static aerodynamic data were obtained.

The dimensions of the 75% scale model are defined as $0.1095 \times 0.1095 \times 0.0194$ m for the base plate, $0.1181 \times 0.0435 \times 0.0561$ m for the battery block on top with a 0.0076 m overhang in the aft, $0.1092 \times 0.0158 \times 0.0158$ m for the arms with the length being measured from the corner of the base plate to the center of the rotor mounts, and the rotor mounts are a cylinder with a radius of 0.0167 m and a height of 0.0643 m. The vehicle's reference length (l_{ref}) was defined as the non-diagonal distance between rotor hubs at 0.2663 m. The reference area, A is computed as the square of the reference length.

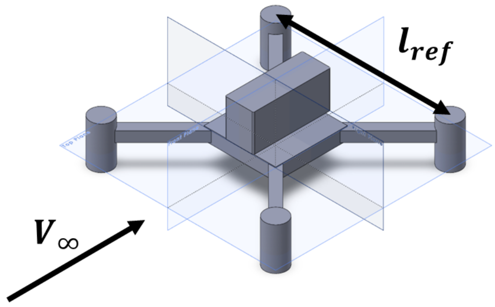

Figure 1: CAD of the quadrotor vehicle.

3.1. Experimental Methods

The DEVCOM ARL wind tunnel is a closed loop, low-speed wind tunnel with force and flow field measurement capabilities at small UAV scales. A series of wind-tunnel tests were conducted on a set of representative quad-copter shapes, an example of which is shown mounted in the wind tunnel in Fig. 2. The airframe geometry was constructed of simple shapes which were representative of typical quad-rotor airframe geometry. A set of three models of different sizes were tested at a variety of angles, up to α = 45° in angle of attack and yaw angles of β = 45°. The shape of the models was held constant but the size was increased to evaluate any scale effects or blockage effects during testing. Flow velocities of 5–20 m/s were evaluated to determine any Reynolds number effects present in the data. An ATI Nano 25 6-axis load cell was used to collect aerodynamic forces with 2000 samples recorded at 1 kHz for each pitch/yaw angle tested.

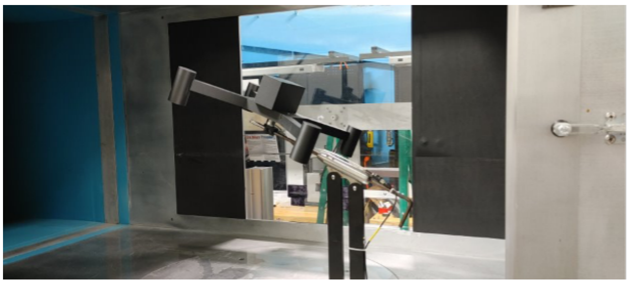

Figure 2: ARL quadrotor vehicle in wind tunnel.

Flow field information was collected using Particle Image Velocimetry (PIV) and data were captured and processed using LaVision's DaVis 10 software. Images were recorded using a Phantom v641 high speed camera equipped with a Nikon Nikkor 50 mm. The cameras have 4-megapixel CMOS sensors with 2560 pixel $\times$ 1600 pixel resolution at the recording frequencies used. Based on the lens and camera setup the approximate field of view of the final data was 50 cm by 30 cm. Aerosolized oil droplets approximately 1 μm in diameter were illuminated using a Photonics Model DM dual head high-speed Nd-YLF laser, which produces 527 nm illumination at approximately 100 mJ/pulse. Sheet optics were used to form a laser sheet on the center-line of the quad frame.

Images were recorded at 500 Hz to capture transient flow phenomenon with 1000 image pairs. The delay time between image pairs was selected to maintain a maximum particle displacement of less than 10 pixels between images. Image pairs were processed using LaVision's GPU processing method, which uses multiple decreasing interrogation windows. A final interrogation region of 12 $\times$ 12 pixels with 25% overlap was used in this study. Uncertainty for the vectors was calculated in DaVis using the methods described and validated by Wieneke (Ref. 28) and was found to be between 1.5% to 3% of the free stream speed. Post-processing of the flow fields was performed in Matlab using the method described in Cohn (Ref. 29) to fit the data onto a regularly spaced grid with data spacing of 3 mm. Vorticity was calculated using velocity vectors on this regular grid.

3.2. Low-Fidelity M & S Solver (GTABB/COMPASS)

The impact of the different aerodynamic vehicle loads were quantified in a real-time modeling and simulation code developed for vehicles that includes the ability to evaluate separated, unsteady flows. The approach, the Georgia Tech Aerodynamics of Bluff Bodies (GTABB), was originally developed for the assessment of dynamic sling loads (Ref. 26), but has been successfully applied to UAVs (Ref. 15, 30) and independently validated (Ref. 31). GTABB was developed from unsteady aerodynamics equations and can be applied to both static and dynamic motion of the vehicle. Unlike higher fidelity methods, GTABB provides time-domain predictions of the vehicle forces and moments during simulated flight and maneuvers.

The GTABB M&S solver requires that the forces and moments of the UAV be defined over the range of orientations in the yaw and angle of attack under consideration. These data can be obtained through a variety of means including wind tunnel tests and computational fluid dynamics (CFD) (Ref. 15). As these approaches require investment in time and money that can be prohibitive to some of its applications, an alternate approach has been developed to provide these quasi-steady data. The COMPlex Aerodynamic Shape Simulator (COMPASS) is a reduced-order model that can be used to construct the behavior of more complex vehicle shapes from canonical shapes, such as rectangular prisms and cylinders (Ref. 27, 32). This approach has been demonstrated to be more accurate than an assumption of equivalent flat plate drag and within 5%-10% of data obtained from CFD (Ref. 17). For full maneuverability, COMPASS produces a complete range of attitude orientations of quasi-steady aerodynamic force and moment coefficients across the α values of -180°to 180°, and β values of -180°to 180°.

3.3. Mid-Fidelity Solver (Lattice–Boltzmann Method)

The mid-fidelity aerodynamic solver is based on a Lattice–Boltzmann method (LBM) and is capable of modeling unsteady flow physics around the vehicle. OpenLB (Ref. 33), an open-source C++ library was utilized for this paper, with GPU acceleration initially implemented by students at the Technical University of Munich and further developed by students at the Georgia Institute of Technology. The Bhatnagar-Gross-Krook (BGK) dynamics model (Ref. 34) for particle population collisions and the Smagorinsky turbulence model with a Smagorinky constant value of 0.1 was used.

A uniform flow inlet of a given freestream velocity was prescribed using an equilibrium boundary condition, which sets all the particle populations at the inlet cells to an equilibrium state corresponding to the given inlet velocity. A pressure boundary condition was assigned to the outlet and a slip boundary condition was applied to the flow domain's remaining four faces. Finally, the grad immersed boundary condition (Ref. 35) was applied to capture the true surface of the vehicle in the voxelized grid.

The computational flow domain was defined to be $4l_{ref}$ in the freestream direction, with the vehicle's origin placed at 37.5% of the domain from the inlet to better capture the wake. In the remaining two directions, $3l_{ref}$ was used, with the vehicle being placed at the center. A visualization of the LBM simulation domain is shown in Fig. 3. Aerodynamic loads were recorded at 1 kHz and the flow field data was saved at 500 Hz corresponding to the experimental setup.

A domain size study was performed to study the effects of using a larger domain by extending the domain in the wake direction only, and also by extending it in all six directions. No significant changes were observed in these tests and, therefore, the aforementioned domain size was used for all LBM results shown in this paper in the interest of computational efficiency. A rigorous grid convergence study was also performed for the baseline orientation (α = 0°, β = 0°) at the flight speed of 20 m/s. The final grid size was chosen to have 200 grid points per l_{ref}, resulting in a Cartesian grid of 288 million nodes. The convergence criterion required that the vehicle lift and drag not vary more than 2% over a one-second interval. The GPU-accelerated LBM solver was able to compute the solution in 3.5 hours using a local NVIDIA DGX A100 40GB system with eight GPUs.

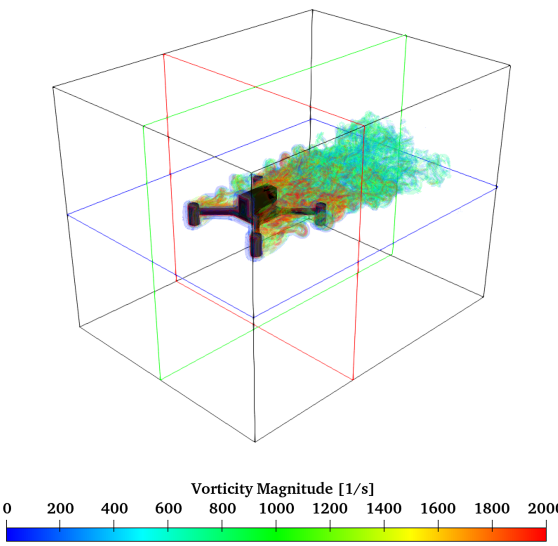

Figure 3: LBM simulation domain with Q-criterion contours colored by vorticity magnitude and planes denoting the center of the vehicle.

3.4. High-Fidelity Solver (FUN3D)

The high-fidelity solver used was FUN3D, a fully unstructured uRANS solver developed at the NASA Langley Research Center. FUN3D has been validated for a variety of incompressible applications for rotorcraft, bluff bodies, and many other structures (Ref. 26, 36). This high-fidelity solver provides many turbulence diffusion models, and for the purposes of this paper, a Spalart-Allmaras Delayed Detached Eddy Simulation (SA-DDES) turbulence closure is applied to resolve the bluff body wake aerodynamics. A stable blend of second- and third-order backward difference formulae (BDF) provides time-accurate temporal integration.

An initial mesh (M1), based on prior bluff body mesh experience, was developed to obtain preliminary force and moment data. The computational domain for this mesh was a sphere with a radius of 10 times the drone reference length, comprising of approximately 10.4M

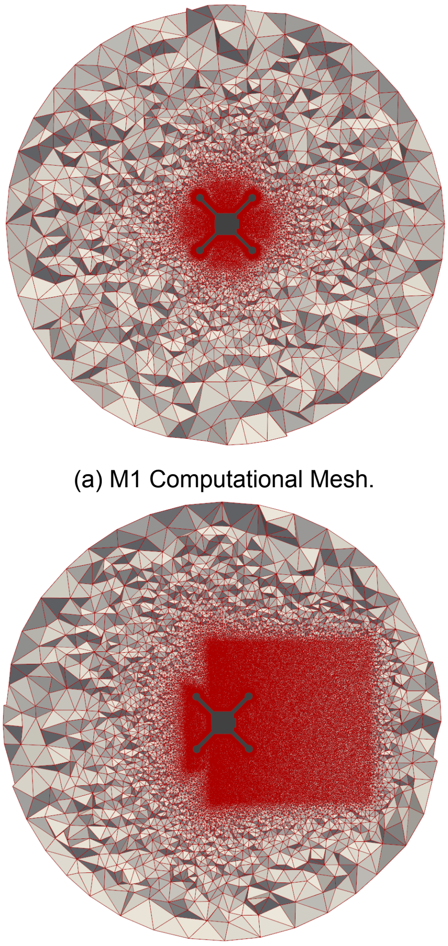

(a) M1 Computational Mesh.

(b) Refined M2 Computational Mesh.

Figure 4: Top-down views of a waterline slice through the computational domain of the two uRANS meshes. Cell edges are colored red.

volume cells. Sources of additional volume cell refinement between the rotor arms were included to more accurately capture flow features in these areas. Additional cell refinement was added in the off-body wake of the drone body to ensure vorticity does not breakdown in the immediate wake beyond the aft rotors for flow field visualization and to verify the mesh airload accuracies. The new computational domain (M2) contains 32.7M volume cells and a surface $y^+ \leq 1.0$ has been ensured, based on the most restrictive cases anticipated. Results from both M1 and M2 meshes are included for the force and moment predictions, and M2 results have been utilized for the flow field visualizations. A comparison of the refinement differences in the initial and final grids with a top-down planform view are provided in Figure 4.

Time-accurate simulations were performed with a time step of 6.667×10^{-4}, equivalent to 20 timesteps per l_{ref}, with 10 subiterations to ensure computational convergence of 4 orders of magnitude at each time step. Airloads and flowfield data were saved at frequencies comparable to the experimental data collection. Convergence was considered achieved when the averages of the lift and drag coefficients varied less than 2% between one-second intervals. This typically occurred within 4.5 – 6 seconds for the angles of attack and yaw evaluated.

The simulations were computed on either 1256 or 2560 processors on the Department of Defense High Performance Computing (DoD HPC) clusters, resulting in a second of unsteady data produced on the M2 mesh in 2.56 or 1.26 hours, respectively.

4. RESULTS

4.1. Forces and Moments

The relevant forces and moments associated with the sweeps in angle of attack and yaw are evaluated. Specifically, lift (C_L), drag (C_D), and pitching moment coefficients (C_{M_y}) for angle of attack sweeps at yaw angles of 0° and 90°, as defined by the freestream in Fig. 1. The orientation as depicted in Fig. 1 is a yaw angle, β = 0, while a clockwise rotation about the normal (z) axis yields the 90° orientation.

The plots compare all levels of numerical results, from the early design (GTABB) to modeling and simulation (LBM) to analysis (FUN3D) levels, compared with the experimental data. The dashed lines indicate the standard deviation of the experimental data, averaged over a two-second interval at 1 kHz, and provide a reference of the variability of the measurements. While both LBM and FUN3D data were also averaged over the same time interval and frequency as the experiment and thus also include standard deviations, they are not included for readability. COMPASS provides only a single coefficient value at each orientation.

Within the bounds of the experimental sensitivity, the uRANS (M2 refined mesh) and LBM approaches predict lift and drag coefficients, Figs. 5a and 5b, for most of the angles of attack evaluated. As might be expected, this is not the case for the very small values associated with pitching moment, but the trends observed in experiment are captured by both LBM and uRANS, as depicted in Fig. 5c.

For low negative angles of attack, there is a difference in the experimental and numerical predictions for lift coefficient, observed from -10° to 10° in Fig. 5a. There is an experimental lift peak at -10°, which is also seen in the uRANS M2 predictions, but which is delayed until 0° by LBM. The subsequent decrease in lift as angle of attack increases continues until 5° for

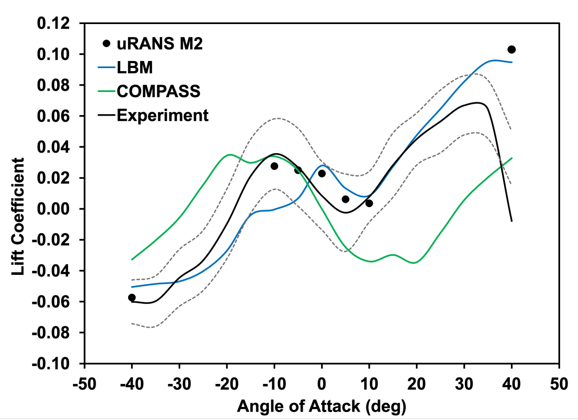

(a) Lift Coefficient

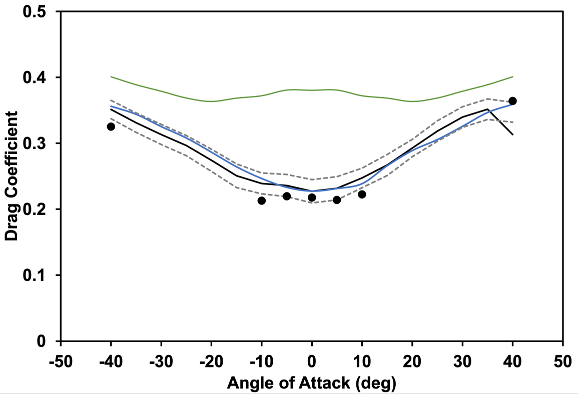

(b) Drag Coefficient

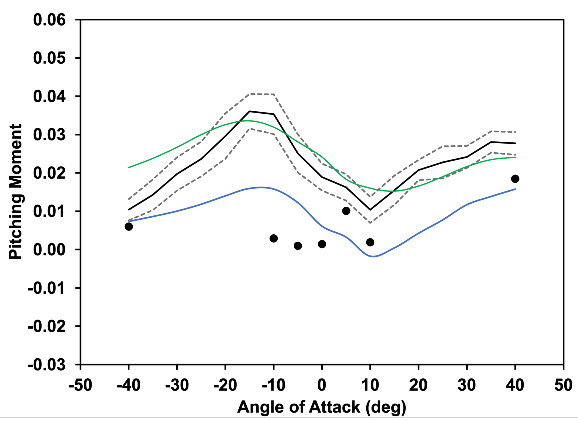

(c) Pitching Moment Coefficient

Figure 5: Aerodynamic coefficient variation for a range of angle of attack at a yaw angle of 0°. All data obtained at five degree increments are depicted as lines, while the more sparse uRANS data are presented as discrete points. The experimental data is bounded by its standard deviation, depicted as the two dashed lines.

experiment and 10° for LBM and uRANS M2. After this minimum, all predictions show a rapid increase in lift.

COMPASS, the low-fidelity approach, exhibited much less success in capturing the lift and drag coefficients, as might be expected. For this effort, the mid-body (fuselage) was modeled as a simple prismatic body encompassing the overall dimensions of the battery plus the base plate. This larger overall area gives rise to the larger drag observed in Fig. 5b, although a drag bucket and increase in drag with angle of attack are observed. This modeling simplification also explains the larger "valleys" observed in the lift coefficient Fig. 5a, though overall the trends are well captured.

The UAV was next rotated 90° clockwise (in yaw) to the freestream and this angle of attack variation repeated. This orientation presents a different windward face with respect to the freestream velocity as the battery overhangs the base plate on the starboard side. Overall similar conclusions for the force and moment data at this yaw angle, shown in Figs. 6a, 6b and 6c. In addition to the refined M2 mesh, the uRANS CFD simulations were performed over a larger set of angles of attack using the original M1 mesh.

The influence of the yaw angle is particularly noticeable for the lift coefficient, Fig. 6a, where the double peaked lift curve is now comprised of a single valley over the range of angles of attack. The COMPASS predictions still present the double peak, and this aids in identifying that the difference arises from the battery overhang and its interaction with the other vehicle components.

The uRANS M1 and M2 mesh data present overall comparable lift coefficient results, indicating a relative invariance with increased wake mesh refinement, which primarily influences separation on the leeward side of the battery and base plate. While both the uRANS M1/M2 and LBM data are again within the bounds of the experimental data for negative angle of attack, differences appear with respect to experiment for positive angles of attack. In particular, the differences are observed over α = 0° – 20°. This was somewhat surprising considering that the configuration is sharp-edged, driving the separation location.

The experimental results indicate that the lift continues to moderately decrease from low negative angles of attack to approximately 20° before increasing. Both the uRANS and LBM lift predictions follow the trend observed in experiment, but reach a minimum at about 5° before rapidly increasing.

The drag coefficients at a yaw of 90° (Fig. 6b) has a small but consistent reduction as negative angles of attack approach zero, and this trend continues to approximately an α=20°, similar to the lift trend. The shape of the drag curve is different from that at a yaw

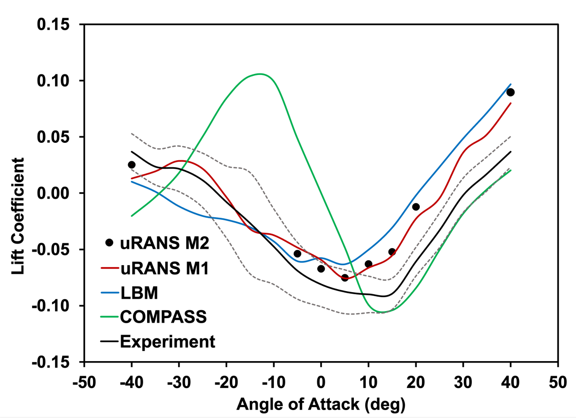

(a) Lift Coefficient

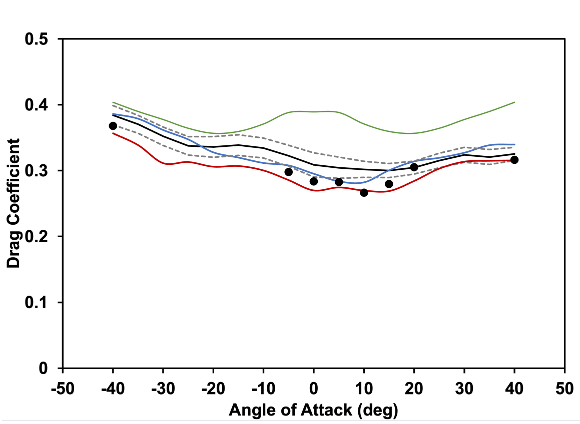

(b) Drag Coefficient

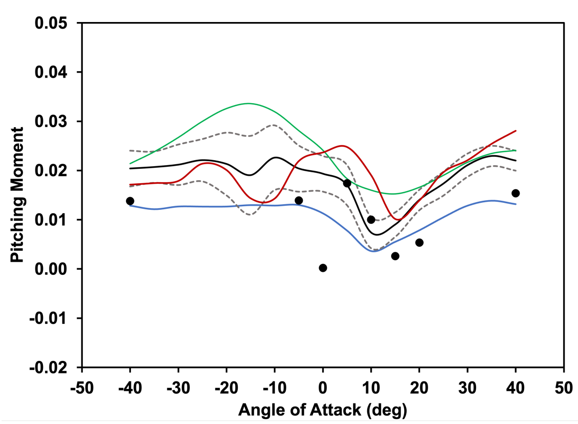

(c) Pitching Moment Coefficient

Figure 6: Aerodynamic coefficient variation for a range of angle of attack at a yaw angle (clockwise positive) of 90°. All data obtained at five degree increments are depicted as lines, while the more sparse uRANS data are presented as discrete points. The experimental data is bounded by its standard deviation, depicted as the two dashed lines.

of 0° (Fig. 5b), and the overall drag values are increased by about 1/3. The LBM and uRANS M1/M2 mesh drag coefficients follow the predicted trend overall, except the increase drag rise begins at about α=10°, which is slightly behind their predicted lift coefficient prediction, but still before the experimental prediction. A difference between the uRANS M1 and M2 meshes can be observed, indicating that the refined mesh provides more accurate drag predictions, though they still remain below that of the experiment.

The pitching moment predictions with ninety degrees yaw (Fig. 6c) are also relatively comparable to the observations without yaw (Fig. 5c). One main difference is that the uRANS M1 mesh data, when corrected to the same reference location as the LBM and experiment, provides a much better prediction than that observed by the uRANS M2 mesh, inferring a strong sensitivity to computational evaluations.

A final observation is that the COMPASS force predictions falls outside the experimental data bounds over a significant range of angles of attack due to the assumption of the single fuselage body element. Interestingly, the COMPASS pitching moments, both in trend and magnitude, do fall within the experimental bounds for a large portion of the angle of attack range.

4.2. Physics at Low Angles of Attack

The discrepancies in the lift coefficient behavior between experimental and computational (LBM and uRANS) at low angles of attack for a yaw angle of 90° warrant further investigation. Unfortunately, the experimental data consist of PIV wake flow field planes and load cell aerodynamic data, and the LBM analysis, by definition, does not include surface data.

While the differences cannot be explained without additional experimental data, some insights can be gained by examining the uRANS results. The surface pressure coefficients from the uRANS M2 mesh analysis was determined to provide a clearer picture of the vehicle force and moments.

At a yaw angle of 90°, the uRANS and LBM indicate that the minimum lift and drag coefficients occur at α=5° and α=10°, respectively, rather than the 20° of experiment. To elucidate this behavior, orthogonal views of the fore and aft vehicle surface, colored with pressure coefficient C_p, depicted in Fig. 7. The freestream velocity vector is aligned along the positive x-axis, with an increasing component along the positive z-axis as the angle of attack increases. Thus, the velocity vector is oriented from the lower left corner of the left column of plots, and the lower right corner for the right column of plots. The left column shows the windward side of the vehicle, which has pressure coefficients near or at the stagnation point (dark red), while the right column provides the leeward side of the

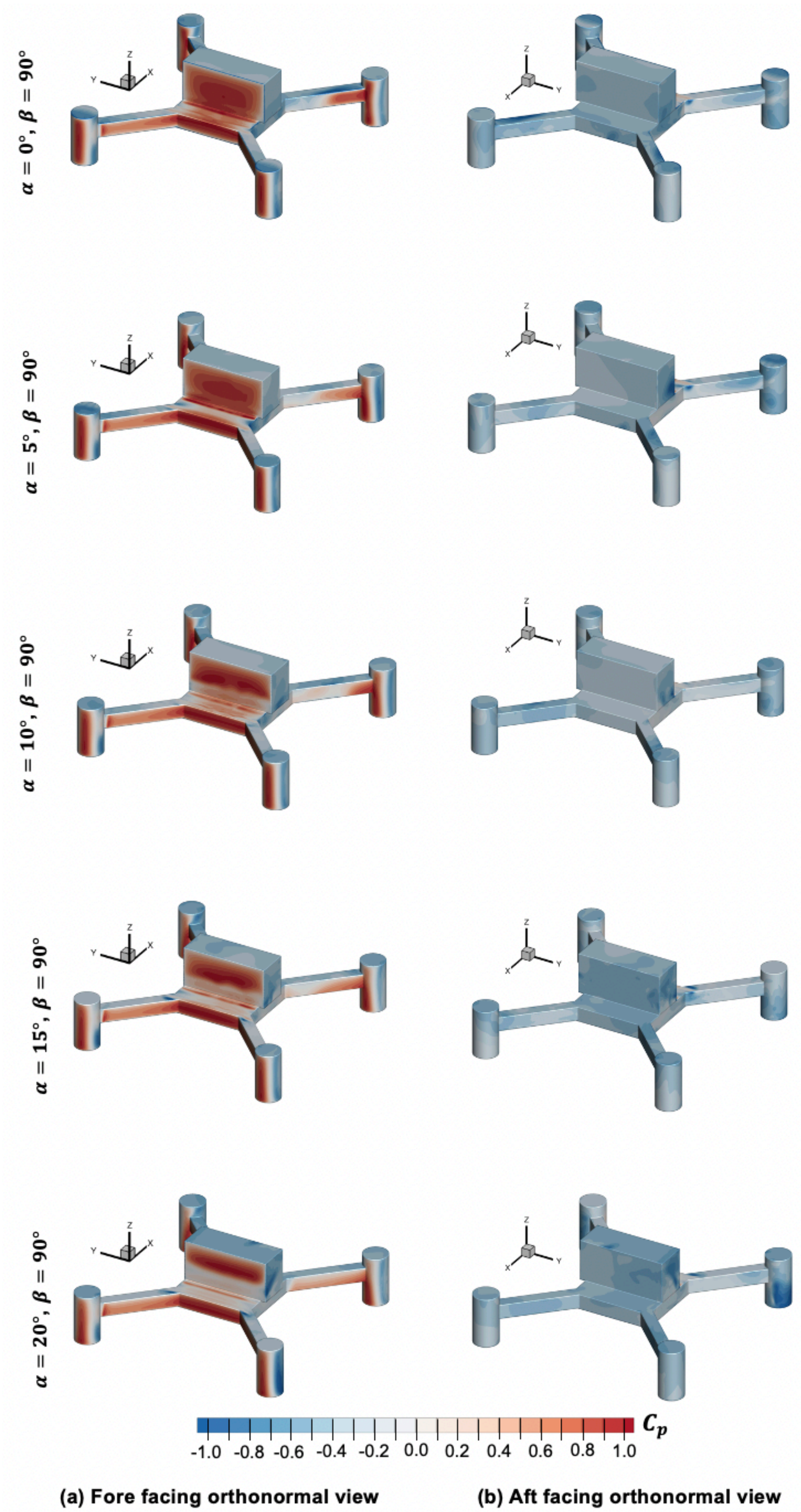

Figure 7: Fore and aft views of the distribution of uRANS predicted surface pressure coefficient at low angles of attack at a yaw angle of $\beta = 90°$, as predicted with the M2 mesh.

vehicle, where suction (dark blue) occurs. Freestream pressure coefficient (C_p=0.) is not colored. The angle of attack increases from α=0° at the top of the page to α=20° at the bottom, in increments of α=5°.

At α=0° the windward (forward) side of the base plate/battery, as well as the arms and rotor mounts, all exhibit the maximum areas of stagnation pressure, while the leeward (aft) side indicates separated flows by light blue colors. As the angle of attack increases, the windward side of the vehicle tips upward, creating a shear layer where the stagnation pressure decreases and flow separates, as indicated by the region of dark red changing to light red and light blue.

On the leeward (aft) side of the vehicle, the larger regions of separated flow (light blue) with smaller zones of suction (darker blue), gradually change to larger zones of suction with smaller regions of separated flow.

The key to the changing aerodynamic response lies with planes orthogonal to the windward and leeward vehicle surfaces. The normal ($x - y$ plane) faces of the vehicle indicate primarily separated flows at these angles of attack with some small zones of increasing suction as the colors become darker blue as the angles of attack increase. While the bottom surfaces are not depicted, the influence of their behavior can also be extracted by the changing pressures along the lower portion of the leeward surfaces. Suction around the lower aft edge of the base plate becomes more apparent at and above α=10°, resulting in the increased drag.

The lift behavior requires the analysis of the side ($x - z$) surfaces. The starboard side of the vehicle (right side of the forward facing view in the left column) indicate the presence of a distinct vortex forming from the intersection of the battery and base plate. The presence of the vortex is clear at α=10°, while not present at lower angles of attack. The trajectory of the vortex increases and gains strength (blue region expands and color deepens) as the angle of attack increases. The influence of the vortex is also observed on the port side surfaces of the aft facing (right column) views. The influence of these vortices on the leeward and top sides of the vehicle is reflected in the increased suction as the vortex reaches the aft end of the vehicle sides.

The role of the motor arms and mounts appear to be less significant. The pressure coefficient distributions indicate increased pressure coefficient on the windward side of the aft arms at $\alpha \geq$10°, along with increased suction on the lower half of the forward motor mounts.

It can therefore be inferred that the drag begins to increase after $\alpha \geq$10° due to the increasing frontal area of the base plate. The angle of attack introduces a vortex emanating from the battery/base plate intersection, which increases in magnitude with angle of attack and is aided by the suction on the lower portion of the forward motor mounts.

Given the findings here, it is likely that differences between the numerical and experimental data reside in the interactional effects of the model and tunnel mount. Per Fig. 2, where the UAV is in the β=90° orientation, the sting is mounted in the middle of the bottom surface of the vehicle. Thus, during the critical time when angles of attack are increased from level flight to 20°, the circular shape of the sting mount will disrupt the flow and introduce a vortex along the lower surface. This action will continue to reduce the lift and drag until the effects of the upper portion of the UAV dominate the flow field, which can be inferred to be at an α=20° for this yaw configuration. Computational analyses that include the sting will aid in confirming this hypothesis, but are planned as a future research effort.

4.3. Flow Field Analysis

Fig. 8 shows instantaneous vorticity contours for α=40°, β=0° and α=40°, β=90° cases and good agreement was observed between all three methods for both yaw angles. The angle of separation was similar for all three with the exception of the top surface for uRANS at α=40°, β=0°. This appears to be different due to the particular time step being visualized, as evident from the time-averaged flow field comparison shown in Fig. 9. The lower separated shear layer, observed in the uRANS and LBM results was not as easily viewed in the experimental results. This was likely caused by the experimental mounting hardware. It should be noted that the slice of the drone model shown in the PIV results in Figs. 8 and 9 was added during post-processing to visualize the orientation of the drone in flow and is not an exact representation of the model due to the PIV blockage.

Comparing uRANS and LBM, it appears that LBM has a more refined wake detail; however, closer inspection indicates that the vorticity in the uRANS wake tends to be present, but more diffusive. The LBM simulations used a uniform grid spacing for the entire domain and, therefore, they were unable to capture the boundary layer as opposed to the uRANS method with a finer mesh close to the surface of the body, with stretching into the wake. This difference in grid density near the body resulted in the thicker vortex layer shown by LBM on both the top and bottom surfaces of the vehicle.

Further comparing uRANS and LBM, large vortex structures of same rotational direction were shed from the bottom surface of the drone base plate, as predicted by both solvers. These structures were similar in size and intensity, but the LBM solver predicted smaller vortical structures at higher intensity in the direct wake behind the drone body. This difference may be for multiple reasons such as differences in grid density, time-step size or turbulence models, and these potential causes will be investigated further.

Fig. 9 illustrates vorticity contours that were time averaged over one second, for the same flow conditions and vehicle orientation as the instantaneous flowfields in Fig. 8. Both computational methods agreed well with the experiments, with the same (previously discussed) mounting hardware interference observed in the time average. The time-averaged contours also show a slightly slower diffusion of the vehicle wake predicted by LBM, which was already pointed out when analyzing the instantaneous flow fields. uRANS more closely mimics the windward recirculation zone at the plate and battery observed by PIV. Here, the LBM recirculation zone is stronger and higher than PIV and uRANS.

The shadowing of the battery block behind the base plate for the α =40°, β=90° case and the associated recirculation region can be observed in the measurements and the two computational flow field predictions. A second angle of separation can be observed from the top front edge of the battery block for all three methods. The results indicate that both uRANS and LBM are able to capture the general flow topology and larger-scale coherent flow structures accurately, as also evidenced by the agreement in force and moment coefficient values.

Figs. 10 and 11 compare the time-averaged and instantaneous vorticity contours, respectively, in the waterline center plane for the baseline orientation (α = 0°, β = 0°) for uRANS and LBM. Both computational methods predict the vortex shedding from the rotor hubs. Similar to the results for the buttline plane discussed previously, the uRANS method captured the structure of boundary layer and near-wake in greater detail, while the LBM simulations captured the far-wake in greater detail. Fig. 11 further illustrates that both solvers were able to capture the overall flow topology.

4.4. M&S Sensitivity to Aerodynamic Predictions

While these analyses have provided insights into the capabilities of the different numerical approaches compared to the accuracy of experimental data, a

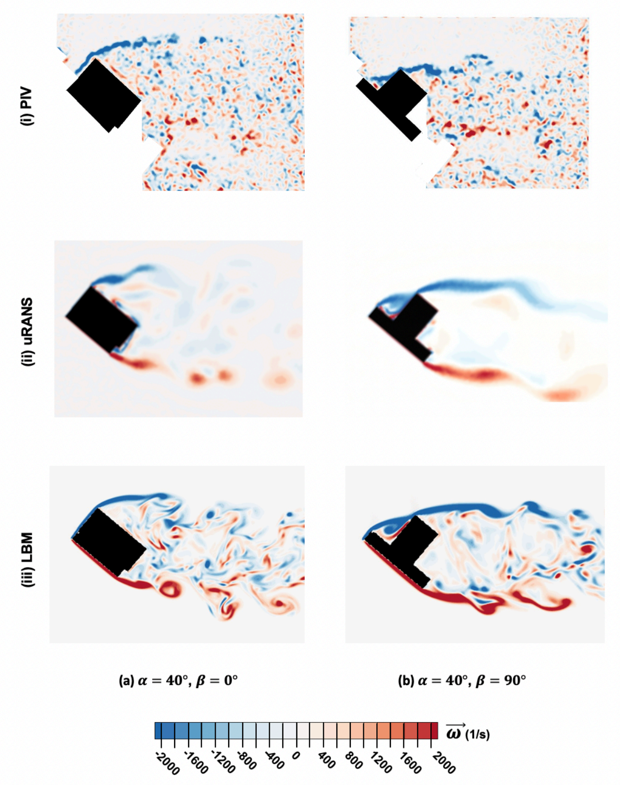

Figure 8: Instantaneous flow field realizations for buttline plane showing out-of-plane vorticity for two yaw angles.

number of use cases would benefit from the reduced costs of LBM or a reduced-order model. The forces and moments from the analyses computed at the angles of attack and yaw were integrated into the quasi-steady database necessary for the GTABB simulations. The analyses were limited to the angles of attack between -40° $\leq \alpha \leq$ 40° , while the -10° $\leq \beta \leq$ 130° were combined using symmetry to provide a much larger coverage. Data were interpolated where gaps existed, in particular for the more costly uRANS data. All force and moment data from the predictions and experiment were integrated in the database, although not all of them have been illustrated in this paper.

The UAV was commanded to avoid a circular obstacle 3 m in diameter after flying 100 meters by performing a yaw maneuver. The vehicle was commanded to avoid the obstacle with a coupled roll and yaw maneuver, returning to its original altitude and 20 m/s flight speed as soon as possible. The results were verified to fall with the limits of the angle of attack and yaw data available. As results between this and a similar pull-up maneuver were similar, only the yaw maneuver result is presented. The trajectories predicted using the experimental data form the reference to which the other results are compared.

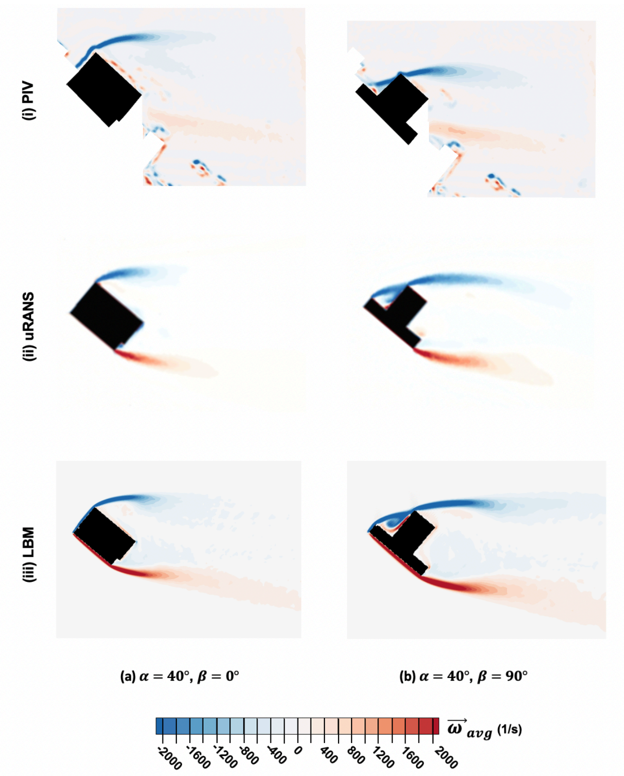

Figure 9: Time-averaged flow field realizations for buttline plane showing out-of-plane vorticity for two yaw angles.

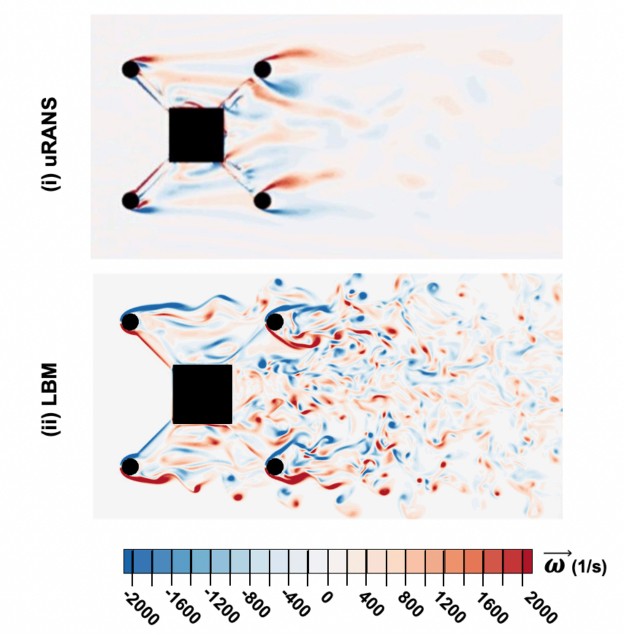

Figure 10: Instantaneous flow field realizations in the waterline plane showing out-of-plane vorticity for two computational methods.

Using the forces and moments, along with the PID controller, the predicted trajectories of the obstacle

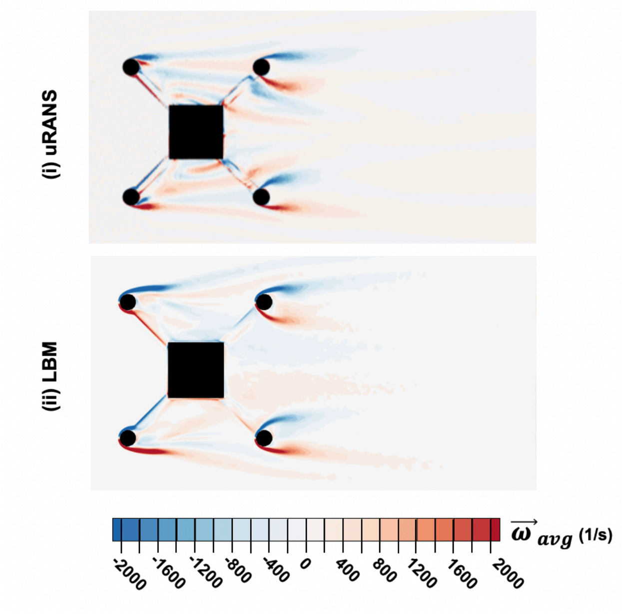

Figure 11: Time-averaged flow field realizations in the waterline plane showing out-of-plane vorticity for two computational methods.

avoidance maneuver using the forces and moments from each source are mapped in Figs. 12 and 13. There are minimal differences in the normal path prediction (0.2 m); the main focus of analysis is for the lateral $(x - y)$ plane, illustrated in Fig. 13.

uRANS and LBM have recovered their flight path by 400 meters after the onset of the maneuver, but the experimental and COMPASS trajectories have a recovery (straight and level flight) delayed by approximately 25–30 m. The combination of the quasi-steady forces and moments from uRANS and LBM simulations render them relatively comparable to the experimental trajectory. The peak-to-peak magnitude of the maneuver is predicted within 5% (0.4 m), 15% (1.1 m) and 21% (1.6 m) by uRANS, COMPASS and LBM, respectively. LBM and uRANS have smaller peak-to-peak magnitudes compared to the experimental predictions, while COMPASS has a larger magnitude. LBM and uRANS accurately predict the vehicle avoidance distance (first peak at approximately 100 m) within 0.5 m of the experiment. All simulations instigate the avoidance turn recovery approximately 5-10 m earlier than experiment.

The flight path recovery after the maneuver bifurcates into two different characteristic paths. The uRANS and COMPASS initiate a near-linear return to the original flight path, while the LBM and experimental approaches perform another yaw turn over 100 meters with minor corrections thereafter.

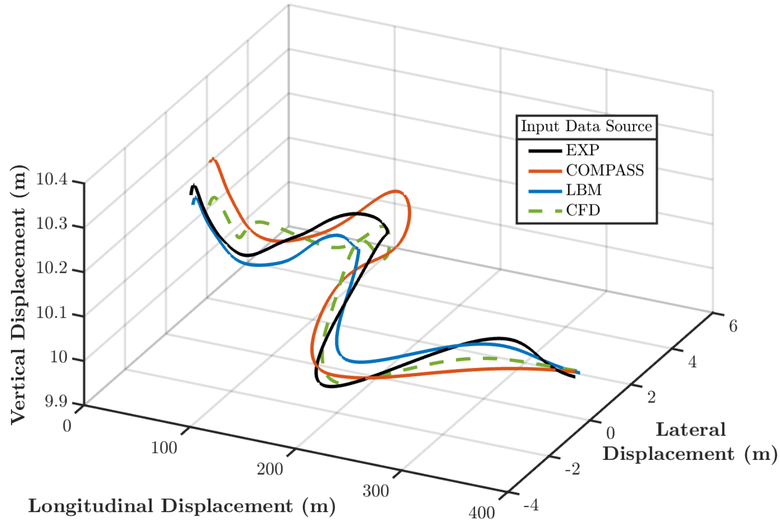

Figure 12: Trajectory of the obstacle avoidance maneuver predicted by GTABB.

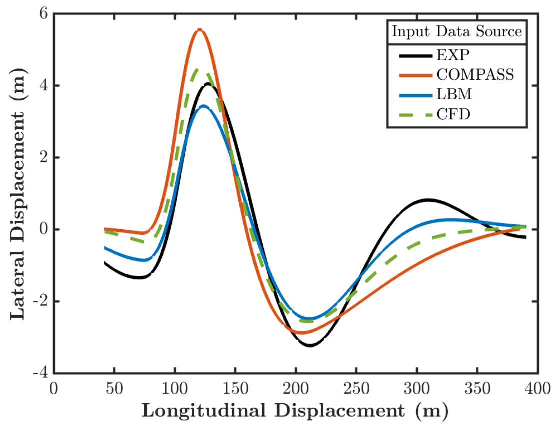

Figure 13: Lateral trajectory of the obstacle avoidance maneuver predicted by GTABB.

5. CONCLUSIONS

A series of numerical analyses have been conducted on an uncrewed aerial vehicle (UAV) over a range of aerodynamic fidelities, from a reduced-order model to a Lattice–Boltzmann Method (LBM) and an unsteady Reynolds-averaged Navier–Stokes (uRANS) simulation with advanced turbulence closures. These numerical results have been compared with one another and a small experimental wind tunnel measurement campaign to understand the capabilities of the mid- and high-fidelity models (LBM and uRANS, respectively) to capture the physics. These results were included in a limited evaluation of a flight maneuver to understand the sensitivity of the forces and moments for design, vehicle flight dynamics and modeling and simulation (M&S) models.

The conclusions of this study include:

- Despite the differences in computational expense, both the LBM and the uRANS methods provided accurate force and moment predictions for the UAV that lie predominantly within the standard deviation bounds of the experimental data.
- The unstructured fully-turbulent uRANS simulations including a delayed detached eddy simulation (DDES) in the wake was evaluated over a limited number of orientations to assess the airloads sensitivity to wake mesh refinement. A mesh with a tripled near-wake resolution had minor influence on the normal forces and moderate influence on the in-plane forces and all relevant moments.
- The reduced-order model, with geometrical sim-

plifications that include a single fuselage (rather than the separate battery and base plate combination) and rectangular (rather than circular) motor mounts, was able to capture the trends of the most relevant airloads. The pitching moment trends and magnitudes were also well captured.

- The influence of the model sting was evident in the delayed lift recovery and drag increase when the vehicle was oriented at the location of maximum yaw influence (β=±90°; only β=90° was examined due to symmetry). The influence of the flow on the lower surface of the base plate was key to the physics, which was disrupted with the sting. The vehicle at β=0° did not appear to be affected by this interaction as the uRANS was able to predict the trends closely with experiment.
- Good agreement of the mean and instantaneous vortical flow field structures was observed between measurements, uRANS, and LBM, with all three methods showing similar angles of flow separation at different parts of the vehicle. The advantages and disadvantages in using each type of computational solver is readily apparent when slices of these flow fields are compared.
- The sensitivity of the UAV to these airloads was evaluated within the M&S code GTABB, which can also be used in design. The use of uRANS and LBM predictions, as expected, predicted a flight path that was arguably the closest to that predicted with experimental data inputs, though their behavior was slightly more favorable than that using experimental inputs. The COMPASS inputs indicated a more conservative response. However, all of the models provided relatively similar responses.

Current endeavors include a refined modeling within COMPASS that includes stacked configurations (battery and base plate) along with cylinders. FUN3D analyses that include the sting and UAV model are planned to confirm the differences in the behavior noted at the β=90° orientation.

6. ACKNOWLEDGMENTS

This effort was partially funded by grant W911NF2120236 from the Army Research Laboratory.

Mr. Oates is supported by a DoD SMART Scholarship, funded by OUSD/R&E (The Under Secretary of Defense-Research and Engineering), National Defense Education Program (NDEP) / BA-1, Basic Research.

The authors would like to acknowledge Walther Chong at the Georgia Institute of Technology who aided in the GTABB simulations.

7. REFERENCES

[1] U.S. Army UAS Center of Excellence Staff, "U.S. Army Unmanned Aircraft Systems Roadmap 2010-2035," , 2022. DOI: https://fas.org/irp/program/collect/uas-army.pdf)

[2] Gavrilets, V., Mettler, B., Frazzoli, E., Piedmonte, M., and Feron, E., "Aggressive Maneuvering of Small Autonomous Helicopters: A Human-Centered Approach," *International Journal of Robotics Research*, Vol. 20, (10), October 2001, pp. 795–807. DOI: 10.1177/02783640122068100

[3] Johnson, E., and Mooney, J., "A Comparison of Automatic Nap-of-the-Earth Guidance Strategies for Helicopters," *Journal of Field Robotics*, Vol. 31, (4), April 2014, pp. 637–653. DOI: 10.1002/rob.21514

[4] Kaufmann, K., Stroer, P., Richez, F., Lienard, C., Gardarein, P., Krimmelbein, N., and Gardner, A. D., "Validation of Boundary-layer-transition Computations for a Rotor with Axial Inflow," , May 13–16 2019. DOI: 10.4050/F-0075-2019-14525

[5] Jung, Y. S., and Baeder, J., "$\gamma - \overline{Re_{\theta t}}$ Spalart–Allmaras with Crossflow Transition Model Using Hamiltonian–Strand Approach," *Journal of Aircraft*, Vol. 66, (3), 2019, pp. 1040–1055. DOI: 10.2514/1.C035149

[6] Hodara, J., and Smith, M. J., "Hybrid Reynolds-Averaged Navier–Stokes/Large-Eddy Simulation Closure for Separated Transitional Flows," *AIAA Journal*, Vol. 55, (6), 2017, pp. 1948–1958. DOI: https://doi.org/10.2514/1.J055475

[7] Hodara, J., Lind, A., Jones, A., and Smith, M. J., "Collaborative Investigation of the Aerodynamic Behavior of Airfoils in Reverse Flow," *Journal of the American Helicopter Society*, Vol. 61, (2), 2016, pp. 032001. DOI: 110.4050/JAHS.61.032001

[8] Hodara, J., *Hybrid RANS-LES Closure for Separated Flows in the Transitional Regime*, Ph.D. thesis, Georgia Institute of Technology, Atlanta, Georgia, https://smartech.gatech.edu/handle/1853/54995, 2016.

[9] Wissink, A. M., Jude, D., Jayaraman, B., Roget, B., Lakshminarayan, V. K., Sitaraman, J., Bauer, A., Forsythe, J. R., and Trigg, R. D., "New Capabilities in CREATE-AV Helios Version 11," , Jan. 11–15 & 19–21 2021. DOI: 10.2514/6.2021-0235

[10] Smith, M., and Moushegian, A., "Dual-solver Hybrid Computational Approaches for Design and Analysis of Vertical Lift Vehicles," *Aeronautical Journal*, Vol. 126, Special Edition 1295, 125th Anniversary Edition (Invited), 2022, pp. 187–208. DOI: 10.1017/aer.2021.108

[11] Chaderjian, N. M., "A Quantitative Approach for the Accurate CFD Simulation of Hover in Turbulent Flow," *Journal of the American Helicopter Society*, Vol. 68, (online), 2023, pp. 042009 (20pp). DOI: 10.4050/JAHS.68.042009

[12] Ozdemir, G., Horn, J., and Thorsen, A., "In-Flight Multi-Variable Optimization of Redundant Controls on a Compound Rotorcraft," Paper AIAA-2013-5165, AIAA Guidance, Navigation, and Control (GNC) Conference, Boston, MA, 19–22 August, 2013.

[13] Cai, G., Wang, B., Chen, B. M., and Lee, T. H., "Design and Implementation of a Flight Control System for an Unmanned Rotorcraft Using RPT Control Approach," Proceedings of the 30th Chinese Control Conference, 2011.

[14] Peng, K., Cai, G., Chen, B. M., Dong, M., Lum, K. Y., and Lee, T. H., "Design and Implementation of an Autonomous Flight Control Law for a UAV Helicopter," *Automatica*, Vol. 45, 2009, pp. 2333–2338.

[15] Afman, J. P., Koukpaizan, N. K., Grubb, A., and Smith, M. J., "An Enhanced Prediction Methodology for Rapid Performance and Control Design of Highly Maneuverable UAVs," Proceedings of the 43rd European Rotorcraft Forum, Milan, IT, September 12–15 2017.

[16] Voskuijl, M. and Van Tooren, M. J. L. and Walker, D. J., "Condition-Based Flight Control for Helicopters: An Extension to Condition-Based Maintenance," *Aerospace Science and Technology*, Vol. 42, (4), 2015, pp. 322–333.

[17] Koukpaizan, N., Wilks, A., Afman, P., and Smith, M. J., "Rapid Vehicle Aerodynamic Modeling for Use in Early Design," Proceedings of the AHS Aeromechanics Design for Transformative Vertical Flight Conference, San Francisco, CA, January 16–19 2018.

[18] Oruc, I., Horn, J. F., Shipman, J., and Polsky, S., "Towards Real-time Pilot-in-the-loop CFD Simulations of Helicopter/ship Dynamic Interface," *International Journal of Modeling, Simulation, and Scientific Computing*, Vol. 8, Dec 2017, pp. 1743005 (25 pp). DOI: 10.1142/S179396231743005X

[19] Moushegian, A., and Smith, M. J., "Aerodynamic Predictions of the Ship-Helicopter Dynamic Interface with a Dual-Solver Hybrid CFD Methodology," Proceedings of the 48th European Rotorcraft Forum, Winterthur, CH, September 6–8 2022.

[20] Moushegian, A. M., *Dual Solver Computational Modeling of Ship-Helicopter Dynamic Interface Aeromechanics*, Ph.D. thesis, Georgia Institute of Technology, Atlanta, Georgia, http://hdl.handle.net/1853/66581, 2022.

[21] Ashok, S. G., and Rauleder, J., "NATO Generic Destroyer Moving-Ship Airwake Validation and Rotor-Ship Dynamic Interface Computations using Immersed Boundary Lattice-Boltzmann Method," Vertical Flight Society Forum 79, May 16-18 2023.

[22] Ashok, S. G., and Rauleder, J., "Investigation of Interpolation Methodologies for Arbitrary Lagrangian Eulerian Lattice-Boltzmann Formulations with Applications to Real-Time Rotorcraft Flight Simulations," AIAA Aviation Forum, June 27 - July 1 2022. DOI: 10.2514/6.2022-3750

[23] Horvat, H. M., B., and Rauleder, J., "Computational Flight Path Analysis of a Helicopter in an Offshore Wind Farm Using a Lattice–Boltzmann Method," AIAA Scitech Forum, January 11–15 2021. DOI: 10.2514/6.2021-1827

[24] Bludau, H. M., J., and Rauleder, J., "Validation of a Dynamic Inflow Model Based on a Flight Dynamics Model and a Lattice–Boltzmann Fluid Solver Using Flight Test Data," 43rd European Rotorcraft Forum, September 12–15 2017.

[25] Oates, B., Kurban, E., Smith, M. J., and Rauleder, J., "Evaluation of High- and Mid-Fidelity Computational Fluid Dynamics for Complex Ship Airwake Analysis with New Experimental Data," , May 16–18 2023.

[26] Prosser, D., and Smith, M. J., "A Physics-Based Reduced-Order Aerodynamics Model for Bluff

Bodies in Unsteady, Arbitrary Motion," *Journal of the American Helicopter Society*, Vol. 60, (3), 2015, pp. 1–15. DOI: 10.4050/JAHS.60.032012

[27] Prosser, D. T., *Advanced Computational Techniques for Unsteady Aerodynamic–Dynamic Interactions of Bluff Bodies*, Ph.D. thesis, Georgia Institute of Technology, Atlanta, Georgia, https://smartech.gatech.edu/handle/1853/53899, 2015.

[28] Wieneke, B., "PIV Uncertainty Quantification from Correlation Statistics," *Measurement Science and Technology*, Vol. 26, 2015, pp. 074002 (10pp). DOI: 10.1088/0957-0233/26/7/074002

[29] Cohn, R. K., and Koochesfahani, M. M., "The accuracy of remapping irregularly spaced velocity data onto a regular grid and the computation of vorticity," *Experiments in Fluids*, Vol. 29, 2000, pp. S61–S69. DOI: 10.1007/S003480070008

[30] Koukpaizan, N. K., Wilks. A., Grubb, A., and Smith, M. J., "Reduced-Order Modeling of Complex Aerodynamic Geometries Using Canonical Shapes," Paper AIAA–2018–0420, January 8–12 2018.

[31] Drone Racing League YouTube channel, "Unsteady Drag – DRL Sim 3.0," https://www.youtube.com/watch?v=UNoGxq8pQGE, 2019.

[32] Prosser, D., and Smith, M. J., "Flow Characteristics Around Rectangular Bluff Bodies at Angle of Attack," *Physics Letters A*, Vol. 376, (45), 2012, pp. 3204–3207. DOI: 10.1016/j.physleta.2012.08.041

[33] Kummerländer, A., Avis, S., Kusumaatmaja, H., Bukreev, F., Dapelo, D., Großmann, S., Hafen, N., Holeksa, C., Husfeldt, A., Jeßberger, J., Kronberg, L., Marquardt, J., Mödl, J., Nguyen, J., Pertzel, T., Simonis, S., Springmann, L., Suntoyo, N., Teutscher, D., Zhong, M., and Krause, M., "OpenLB Release 1.5: Open Source Lattice Boltzmann Code. Version 1.5." , April 2022. DOI: 10.5281/zenodo.6469606

[34] Bhatnagar, P. L., Gross, E. P., and Krook, M., "A Model for Collision Processes in Gases. I. Small Amplitude Processes in Charged and Neutral One-Component Systems," *Physical Review*, Vol. 94, May 1954, pp. 511–525. DOI: 10.1103/PhysRev.94.511

[35] Dorschner, C. S. B. F., B., and Karlin, I., "Grad's approximation for moving and stationary walls in entropic lattice Boltzmann simulations," *Journal of Computational Physics*, Vol. 295, April 2015, pp. 340–354. DOI: 10.1016/j.jcp.2015.04.017

[36] Biedron, R. T., Vatsa, V. N., and Atkins, H. L., "Simulation of Unsteady Flows Using an Unstructured Navier Stokes Solver on Moving and Stationary Grids," *AIAA Journal*, Vol. 5093, 2005, pp. 1–17. DOI: 10.2514/6.2005-5093